ACS APPLIED ENERGY MATERIALS

www.acsaem.org Article

Shape Control of Ceria Catalytic Supports for Enhanced Ethanol Reforming in Solid Oxide Fuel Cells

Marina Machado, Lays N. Rodrigues, Vanessa B. Vilela, Tamara S. Moraes, Andre S. Ferlauto, and Fabio C. Fonseca*

Cite This: *ACS Appl. Energy Mater.* 2024, 7, 1766–1776 Read Online

ACCESS | Metrics & More | Article Recommendations | Supporting Information

ABSTRACT: Matching the catalytic activity of nanostructured materials and processing parameters for high-temperature electrochemical devices is a challenge. Controlling the nanoparticle shape has been proposed as an alternative method to stabilize crystalline surfaces to inhibit particle coarsening and sustain catalytic activity after high-temperature treatment. In this study, nickel-based catalysts supported on shape-controlled (nanorods and nanocubes) gadolinium-doped cerium oxide (GDC) were evaluated for the steam reforming reaction of ethanol, aiming at direct ethanol solid oxide fuel cells (SOFC). The morphology of the support was shown to have an important role in the catalytic activity, particularly when heat treatments for fuel cell fabrication are considered. The Ni catalyst supported on the GDC nanorods sustained the highest catalytic activity after heat treatment despite the morphology change of the support at high temperatures. The excellent properties of the shape-controlled materials were demonstrated in SOFC using the Ni-GDC catalytic layer tailored for the operation on anhydrous ethanol at 700 °C. The fuel cell exhibited a stable performance for more than 100 h of continuous operation without any sign of degradation due to carbon deposition. Such a result is an important step toward the stable operation of direct ethanol intermediate temperature solid oxide fuel cells.

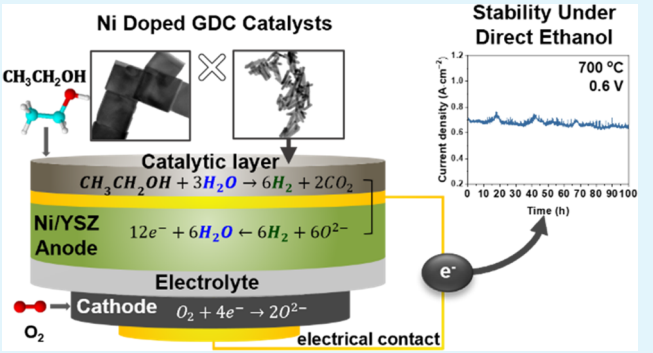

KEYWORDS: *ethanol steam reforming, carbon resistant catalyst, solid oxide fuel cell (SOFC), shape-controlled nanoparticles, direct ethanol SOFC, gadolinium-doped ceria*

1. INTRODUCTION

Solid oxide fuel cells (SOFCs) are efficient electrochemical devices that can run on various fuels contributing to the reduction of the environmental impact of both stationary and mobile power generation.[1,2] Such a contribution is particularly advantageous for the decarbonization of electricity when renewable fuels, such as bioethanol, are considered. Ethanol is the most successful biofuel and plays an important role in the energy transition scenario because it is an efficient liquid fuel that can be obtained from different sources of biomass and is easy to store and transport. Bioethanol is an economically proven viable source of renewable energy in several countries including USA, India, Australia, and particularly Brazil, in which the infrastructure for production and distribution of such high-density energy carrier is available for fueling vehicles countrywide.[3]

Due to the high operating temperature of an SOFC (>600 °C), the direct internal ethanol steam reforming (ESR) reaction (eq 1) is possible.

$$CH_3CH_2OH + 3H_2O \rightarrow 6H_2 + 2CO_2 \quad (1)$$

However, if ethanol is directly fed into the SOFC, carbon will form due to the high Ni content (>30 vol %) of the state-of-the-art Ni/YSZ anode.[4−10] Coke formation on the anode will lead to rapid and irreversible degradation of the fuel cell performance. To overcome such limitation, the addition of a catalytic layer on top of the SOFC anode to promote fuel reforming before it gets in contact with the anode layer has been shown as one of the most promising strategies.[10−16] In this configuration, the catalyst can be tailored to ensure the highest possible fuel-to-hydrogen conversion while preserving the high activity of Ni/YSZ for hydrogen electrochemical conversion. Nonetheless, the catalytic material must meet requirements such as high stability in the harsh processing and operating conditions of an SOFC and be compatible with the other materials in the SOFC.

Received: November 1, 2023
Revised: January 30, 2024
Accepted: January 31, 2024
Published: February 16, 2024

https://doi.org/10.1021/acsaem.3c02757
ACS Appl. Energy Mater. 2024, 7, 1766−1776

Reportedly, supported noble metal catalysts, such as Ir and Rh, exhibit the highest activity toward C−C bond cleavage with negligible coke formation.[17−19] However, for industrial-scale applications, a transition metal catalyst is a more viable option than a noble metal. Low-cost catalysts based on Ni nanoparticles on oxide support, with low Ni content (≤10 wt %), are commonly used as they are relatively stable and have high activity for H_2 production by ethanol steam reforming.[15,20−23] Both metal nanoparticles and the oxide support have important roles in improving ethanol steam reforming. The use of cerium oxide (CeO_2) as a support has been shown to improve ethanol decomposition and inhibit carbon formation.[19] CeO_2 has a high oxygen storage capacity (OSC) due to its double oxidation state, from (IV) to (III), which allows it to release oxygen under reducing conditions and adsorb oxygen under oxidizing conditions. Doping with a trivalent cation, such as gadolinium, creates extrinsic charge compensation defect as oxygen vacancies increasing the mobility of the oxygen species.[24−26]

Additionally, the morphology of the catalyst support has shown to play a role on the Ni dispersion and an increased number of catalytic active sites is expected for high metal dispersion.[27,28] Moreover, in the case of ceria, oxygen vacancy formation is morphology dependent. It has been observed that morphologies such as nanosheets, nanorods, nanocubes have exposed crystalline planes with higher OSC and higher coke resistance.[29,30] Nanowires of Ni/$Ce_{0.9}Sm_{0.1}O_{2-\delta}$ showed increased catalytic activity for ethanol conversion compared to commercial catalyst with the same composition.[31] The increase in activity was attributed to the high surface area of the support, which provided many nucleation sites for the Ni nanoparticles. Similarly, Ni catalyst with CeO_2 supports with different morphologies (nanocube, nanorod, and flower-like) exhibited smaller crystallite size of the impregnated Ni and higher activity for ethanol decomposition as compared to random shaped ceria nanoparticles.[32] Moreover, previous results have shown that controlling the shape of nanostructured materials can favor crystalline planes that can inhibit mass diffusion processes, hindering particle coarsening,[33] which possibly contributes to enhanced catalytic properties.

Along with activity and stability, developing catalysts for ethanol reforming must comply with efforts to decrease the operating temperature of the SOFC. Combining catalytic reactions in this electrochemical device imposes additional challenges at an intermediate operating temperature. At intermediate temperatures (600−700 °C) ethanol dehydrogenation in gas phase reactions results in carbon deposit precursor products, such as ethylene and acetaldehyde. Thus, coke formation in the ethanol reforming is more likely in the 600−700 °C range than at higher temperature. Another crucial aspect that defines the catalyst design for an SOFC is the effect of the fabrication of such ceramic fuel cells on the catalyst properties. High-temperature heat treatments (∼1000 °C) are usually required for the fabrication of functional layers in an SOFC. Thus, the application of a catalytic layer on an SOFC, generally consists of preparing a suspension of the catalyst material with organic additives followed by deposition and heat treatments for both the decomposition of the organic materials (i.e., solvents, pore formers, and organic additives) and the sintering of the layer onto the anode.[13,34−36] Furthermore, the processing steps such as sealing and reduction of the NiO in the anode are typically carried out at a high temperature (≥800 °C).[36,37] Such fabrication and operation steps, mainly the ones at high temperature, affect the microstructure of the catalyst, promoting particle coarsening and mass diffusion in both the ceramic support and the metal that usually impair catalytic properties, resulting in carbon formation and therefore degradation of the fuel cell. Thus, finding strategies to preserve catalytic properties of nanomaterials capable of sustaining high activity after the fabrication and activation of SOFCs is a relevant task.

In the present study, catalysts comprising gadolinium-doped ceria (GDC) with two different morphologies (nanocubes and nanorods) impregnated with Ni nanoparticles (5 wt %) were evaluated for the ethanol steam reforming reaction aiming at intermediate temperature direct ethanol SOFCs. The effect of heat treatment, simulating typical processing of SOFCs, on the properties of nanostructured catalysts, and its use on direct ethanol SOFCs are evaluated.

2. EXPERIMENTAL SECTION

2.1. Synthesis and Characterization of Catalysts. The synthesis of $Ce_{0.9}Gd_{0.1}O_{2-\delta}$ nanorods (GDC-NR) and $Ce_{0.9}Gd_{0.1}O_{2-\delta}$ nanocubes (GDC-NC) was adapted from previously reported synthesis of ceria by a hydrothermal method.[31,38,39] A 14 M aqueous sodium hydroxide solution (NaOH, 99%, Sigma-Aldrich) with 19.6 g of NaOH dissolved in 35 mL of deionized water was transferred to a 100 mL Teflon-lined stainless-steel autoclave. Then, an aqueous 5 mL solution containing 6.2344 g of cerium nitrate ($Ce(NO_3)_3{\cdot}6H_2O$, 99%, Sigma-Aldrich) and 0.7219 g gadolinium nitrate ($Gd(NO_3)_3{\cdot}6H_2O$, 99.9%, Sigma-Aldrich) was gradually added to the NaOH solution under constant magnetic stirring. The autoclave was heated to 110 °C for 24 h to obtain GDC-NRs and to 180 °C for 24 h to obtain GDC-NCs. After the synthesis, the products were washed by five cycles of centrifugation with water and two cycles with ethanol. The synthesized material was dried at 120 °C for 2 h in air and calcined at 500 °C in air for 1 h.[31]

Ni/GDC catalysts were prepared by incipient wetness impregnation of the supports prepared as described above with an aqueous solution of $Ni(NO_3)_2{\cdot}6H_2O$ in order to obtain 5 wt % in GDC-NRs and GDC-NCs. After impregnation, the samples were calcined at 450 °C for 2 h in air flow. The samples after calcination will be further referred to as as-prepared samples. The as-prepared samples were submitted to a heat treatment at 800 °C (5NiGDC-NR and 5NiGDC-NC) and 900 °C (5NiGDC-NR) with a heating rate of 10 °C/min and 1 h dwell time in air for the evaluation of catalytic activity after the heat treatment emulating the sintering of the catalytic layer in an SOFC.

X-ray diffraction (XRD) analyses of the as-prepared powders and the samples submitted to heat treatment at 800 and 900 °C were performed using a Miniflex II model diffractometer with a Cu Kα radiation source (0.15406 nm) in the 2θ range of 20−90°. The average crystallite sizes (D) were calculated with the Scherrer equation using the (111), (220), and (311) reflections. The specific surface area (SSA) of the samples were determined by nitrogen gas adsorption measurements (at −196 °C) (Micromeritics Gemini VII) according to the Brunauer, Emmett-Teller (B.E.T) method. Before the analysis, all samples were degassed under a vacuum at 300 °C for ∼18 h in a Micrometrics VacPrep 061. The elemental analysis of the catalysts was carried out by wavelength dispersive X-ray fluorescence (WDXRF) on a Rigaku Supermini200 spectrometer.

Scanning transmission electron microscopy (STEM) analysis was carried out by a JEOL JEM 2100 instrument operated at 200 kV with a high-angle annular dark-field detector. Samples for STEM were prepared by drop-casting an aqueous suspension of the materials over a carbon-coated copper grid, followed by drying under ambient conditions. Energy-dispersive spectrometry (EDS) analyses of the samples were obtained with a JEOL JEM 1011 instrument operating at 100 kV.

https://doi.org/10.1021/acsaem.3c02757
ACS Appl. Energy Mater. 2024, 7, 1766−1776

Temperature-programmed reduction with hydrogen (H_2-TPR) was carried out in a multipurpose unit with a Pfeiffer Vacuum Prisma detector mass spectrometer. Typically, 0.1 g of catalyst was dried under a He flow at 300 °C for 1 h and then cooled to room temperature. The TPR profiles were obtained between 30 and 1000 °C in a flow of 2% H_2/He, the temperature increasing linearly at a rate of 10 °C·min^{-1}.

2.2. Ethanol Steam Reforming (ESR). ESR evaluation was performed in a fixed bed quartz tubular reactor, 5 mm of inner diameter, packed with 20 mg of catalyst, in a vertical oven at 600 °C. Prior to the reaction, the as-prepared catalysts and the heat-treated catalysts were reduced under pure hydrogen flow (30 mL·min^{-1}) at 450 and 800 °C respectively, for 1 h and then purged under N_2 for 15 min. Water and ethanol were fed into the reactor using a system with two saturators to obtain a fixed stoichiometric H_2O/CH_3CH_2OH molar ratio of 3/1. Nitrogen was used as the carrier gas at a total flow rate of 60 mL·min^{-1}. The ethanol conversion and selectivity of the obtained products as a function of the reaction time were determined by (eqs 2 and 3)

$$X_{\text{ethanol}} = ((n_{\text{ethanol}})_{\text{fed}} - (n_{\text{ethanol}})_{\text{exit}})/(n_{\text{ethanol}})_{\text{fed}} \times 100 \quad (2)$$

$$S_{\text{xl}} = (n_x)_{\text{produced}}/(n_{\text{total}})_{\text{produced}} \times 100 \quad (3)$$

where $(n_x)_{\text{produced}}$ = moles of x produced (x = H_2, CO, CO_2, CH_4, acetaldehyde, or ethylene) and $(n_{\text{total}})_{\text{produced}}$ = moles of H_2 + moles of CO + moles of CO_2 + moles of CH_4 + moles of acetaldehyde + moles of ethylene (i.e., the moles of water produced are not included).

Thermogravimetric (TG) analysis of the samples after the steam reforming reaction was carried out with TA Instruments SDT Q600 equipment. The measurements were obtained between room temperature and 800 °C with a heating rate of 10 °C·min^{-1} under 50 mL·min^{-1} air flow.

2.3. Fuel Cell Fabrication and Testing. The catalytic ink, prepared by mixing the as-prepared 5Ni/GDC-NR + 10 wt % ethyl cellulose (Sigma-Aldrich) with ethanol and polyvinylpyrrolidone (PVP, Sigma-Aldrich, Mw ∼ 55 000), was deposited on an anode-supported button cell by the airbrush technique. The commercial anode-supported fuel cell (Fuel Cell Materials, SKU 213308) is composed of a 8 mol % yttria-stabilized zirconia (YSZ) thin electrolyte supported on the YSZ/Ni composite anode, with a GDC barrier layer and lanthanum−strontium cobaltite cathode. Sintering of the catalytic layer was carried out at 800 °C for 1 h in air. Further details of the contact configuration and catalytic layer preparation are found elsewhere.[11,40] The electrochemical performance of the cell with the Ni/GDC-NR catalytic layer was evaluated at 700 °C in an open flange test setup from Fiaxell SOFC Technologies. Fuel cells were tested under either hydrogen or ethanol using mass flow meters and bubbling a carrier gas (N_2) for ethanol vapor in a temperature-controlled and sealed tank. The total flow on the anode and cathode sides was kept at 46 N ml·min^{-1}·cm^{-2}. The flow ratio of ethanol and hydrogen of 1:6 was chosen for the tests. Such ratio was chosen to carry an equivalent theoretical number of electrons to the anode.[14,36] The stability of the direct ethanol SOFC was evaluated after the initial operation under hydrogen (78% H_2 balanced with N_2) and during continuous operation at 0.6 V under dry ethanol (13% ethanol balanced with N_2).

The electrochemical analyses were performed during cell operation using a Zahner IM6 Electrochemical Workstation. Current−potential (I−V) curves were measured from the OCV to 0.4 V under H_2. Impedance spectroscopy data were collected under polarization at 0.6 V, with 10 mV ac amplitude in the 100 kHz−1 Hz frequency range. The impedance spectra data were analyzed by fitting the distribution of relaxation times (DRT) using the open-source software DRT tools.[41]

3. RESULTS AND DISCUSSION

3.1. Catalyst Characterization. The chemical composition of the catalyst obtained by WDXRF is shown in Table 1. From the results, the calculated Gd/Ce ratio corresponds to the nominal Gd concentration of 10 mol % equivalent to $Ce_{0.9}Gd_{0.1}O_{2-\delta}$. The measured Ni content was ∼4 wt % for both catalysts, slightly lower than the nominal (5 wt %) as inferred from the WDXRF data. The specific surface areas of the 5Ni/GDC-NC and 5Ni/GDC-NR catalysts, both as-prepared and heated at 800 °C, are shown in Table 1. The BET surface area of 5Ni/GDC-NC is considerably lower than that of the GDC-NR. However, the surface area of the nanocubes (∼2 m^2·g^{-1}) has not been significantly changed after heat treatment at 800 °C. On the other hand, the surface area of 5Ni/GDC-NR decreased from 68.8 to 22.3 m^2·g^{-1} after the same heat treatment and further decreased to 11.1 m^2·g^{-1} after heat treatment at 900 °C.

Table 1. Specific BET Area and Chemical Composition of the Catalysts

sample	specific surface area (m^2/g)	chemical composition (wt %)		
		Ni	Gd	CeO_2
5Ni/GDC-NC	2.7	3.6	9.4	87.0
5Ni/GDC-NC (800 °C)		2.0		
5Ni/GDC-NR	68.8	4.4	9.5	86.1
5Ni/GDC-NR (800 °C)	22.3			
5Ni/GDC-NR (900 °C)	11.1			

Figure 1a shows the XRD patterns of 5Ni/GDC-NC and 5Ni/GDC-NR as-prepared and after heat treatment at 800 °C. All diffractograms exhibited diffraction peaks indexed to the ceria cubic fluorite structure corresponding to the solid solution $Ce_{0.1}Gd_{0.9}O_{1.95}$. The 5Ni/GDC-NC catalyst before heat treatment has sharper diffraction peaks as compared to those of 5Ni/GDC-NR, showing that the nanostructured GDC support in the form of nanocubes presents higher crystallinity. After heat treatment, diffraction peaks of the 5Ni/GDC-NC catalyst retain almost the same shape. On the other hand, heating the 5Ni/GDC-NR catalyst at 800 and 900 °C results in sharper diffraction peaks, showing that the heat treatment changed the catalyst nanostructure.

The average crystallite size was calculated by the Scherrer equation for all of the catalysts before and after heat treatment. The calculated crystallite sizes for both as-prepared and heat-treated 5Ni/GDC-NC were 42 nm, evidencing that heating the sample at 800 °C had no effect on the crystalline structure of nanocubes. On the other hand, the as-prepared 5Ni/GDC-NR showed crystallite size of 9 nm, while heating at 800 and 900 °C increased the crystallite size to 15 and 33 nm, respectively.

Figure 1b shows the H_2-TPR profiles of the as-prepared 5Ni/GDC-NC and 5Ni/GDC-NR catalysts. The 5Ni/GDC-NC TPR profile shows four peaks of hydrogen consumption. The first peak at 234 °C, followed by a shoulder at 275 °C, was attributed to Ni reduction with weak and strong interaction with the support, respectively.[8,42,43] The third peak at 612 °C was assigned to the GDC surface reduction and the high-temperature peak occurring at 925 °C was related to the GDC bulk reduction.[44,45] The TPR profiles of both GDC nanorod- and nanocube-supported catalysts, 5Ni/GDC-NR and 5Ni/GDC-NC, respectively, are similar. However, the 5Ni/GDC-NR sample exhibits an additional shoulder at low temperature (160 °C) and broader peaks shifted to lower temperatures than that of the nanocube-supported catalyst. Such features indicate that the morphology of the support affects the reducibility properties and metal−support interactions. The peak at 210 °C

https://doi.org/10.1021/acsaem.3c02757
ACS Appl. Energy Mater. 2024, 7, 1766−1776

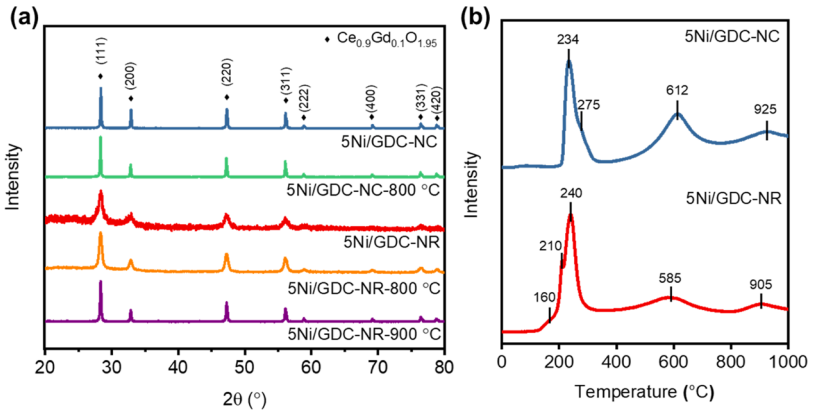

Figure 1. (a) XRD patterns of the Ni/GDC nanorod (NR) and nanocube (NC) supported catalyst before and after heat treatment at 800 and 900 °C, respectivley. (b) Temperature-programmed reduction with hydrogen of as-prepared 5Ni/GDC-NC and 5Ni/GDC-NR catalysts.

was assigned to the reduction of Ni with weak interaction with the support, and the most intense peak at 240 °C was attributed to the reduction of Ni with strong interaction with the GDC support. Similarly, for the nanocubes, increasing the reduction temperature reveals two peaks occurring at 585 and 905 °C that were related to the surface and bulk GDC reduction, respectively. The shift to a lower reduction temperature of the NR catalyst suggests a higher contact between the metal and support and indicates an increase in its reducibility properties and in its oxygen vacancy content.[31,46,47]

The TEM image of the as-prepared 5Ni/GDC-NC (Figure 2a) shows a relatively large distribution of sizes of GDC nanocubes with the edges of the cubes having an estimated length of ∼160 nm. After heat treatment at 800 °C, as shown in Figure 2b, the nanocubes presented comparable shapes and sizes (∼180 nm length); they are slightly more agglomerated and rounded and have a similar size distribution as compared to the as-prepared 5Ni/GDC-NC (Figure 2a). The TEM images of 5Ni/GDC-NR before heat treatment (Figure 2c) show nanorods with a mean length of 80 nm and thickness of 12 nm. After heat treatment at 800 °C (Figure 2d), it is revealed that the GDC nanoparticles retained the rod shape, but rods become more agglomerated, less distinguishable, and clearly larger than those of the as-prepared sample. Further increasing the temperature of the heat treatment to 900 °C, as shown in Figure 2e, completely changed the shape of the 5Ni/GDC-NR catalyst, and the particles assumed a random polyhedron shape having a size of ∼120 nm.

The TEM-EDS maps for 5Ni/GDC-NC (Figure 3a) and 5Ni/GDC-NR (Figure 3b) catalysts after heat treatment at 800 °C show that cerium and gadolinium are homogeneously distributed in both nanorods and nanocube GDC supports. The Ni nanoparticles are clearly observed in the corresponding EDS mapping of Figure 3a,b to have distinct distributions in both samples despite having comparable mean sizes (∼20 nm). In the nanocubes, Ni nanoparticle dispersion seems to be concentrated in nanocube edges and as isolated agglomerated particles, while some cube facets are free of the impregnated metal, as observed in the Ni EDS mapping in Figure 3a. On the other hand, the smaller particle size and larger surface area of the GDC nanorods (Table 1) promoted a higher dispersion of the metal and Ni nanoparticles are observed to be considerably less agglomerated in Figure 3b. Along with the mean particle size of the support, the dispersion of the metal is affected by both the crystalline planes exposed and the surface defects in each nanostructure. The nanorods have defective surfaces that offer effective pinning sites for the impregnated metal nanoparticles, while nanocube faces are well-defined and crystallized. Such crystalline surfaces provide few effective sites for the impregnation of the metal nanoparticles, which are prone to diffuse and agglomerate in the cube edges.[33] Such features observed in the as-prepared samples control the behavior of the samples upon heat treatment and are crucial for their catalytic properties.

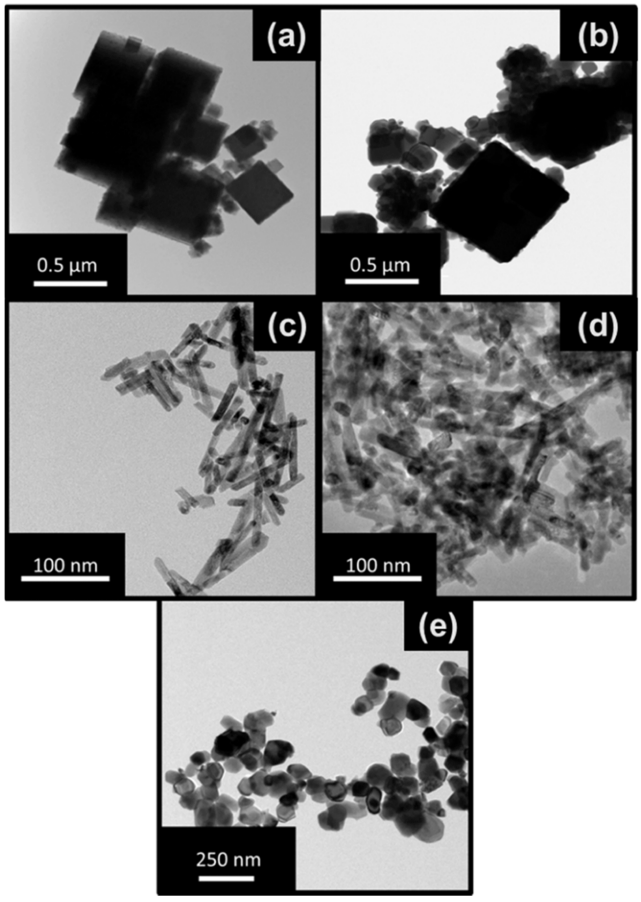

Figure 2. TEM images of (a) 5Ni/GDC-NC as-prepared, (b) 5Ni/GDC-NC after heat treatment at 800 °C, (c) 5Ni/GDC-NR as-prepared, and 5Ni/GDC-NR after heat treatment at (d) 800 and (e) 900 °C.

https://doi.org/10.1021/acsaem.3c02757
ACS Appl. Energy Mater. 2024, 7, 1766−1776

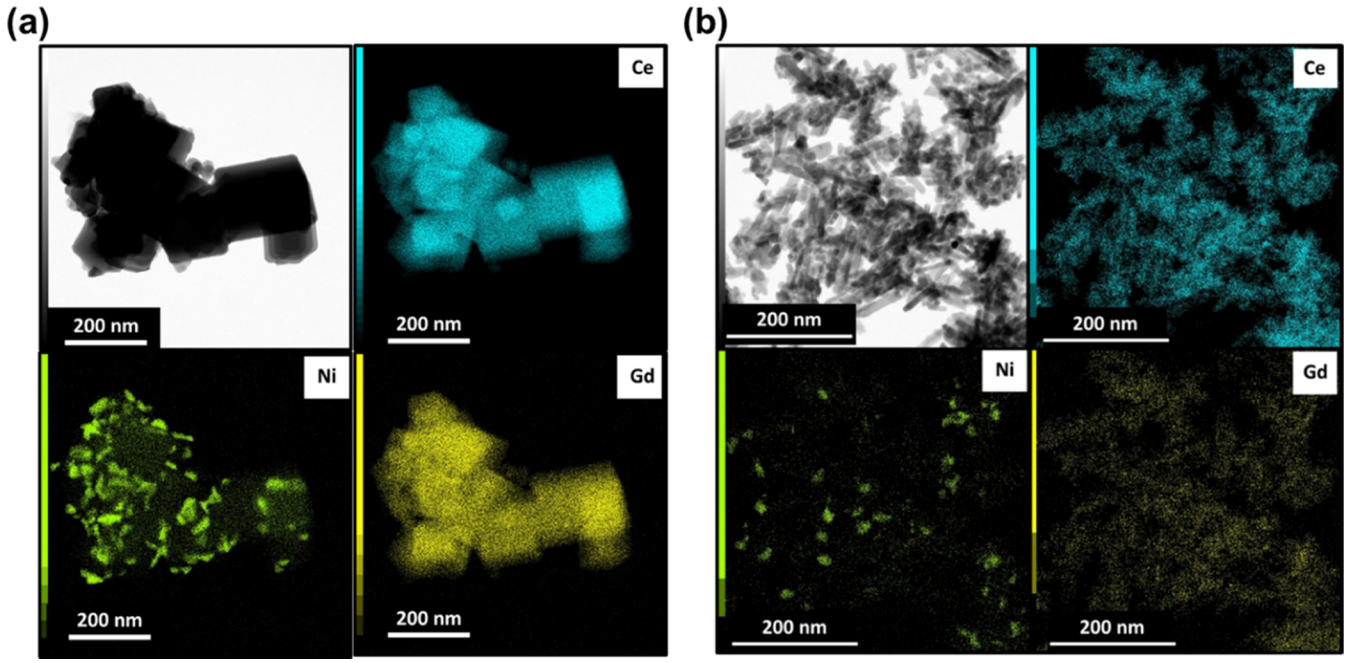

Figure 3. TEM-EDS mapping for the (a) 5Ni/GDC-NC catalyst and (b) 5Ni/GDC-NR catalyst after heat treatment at 800 °C.

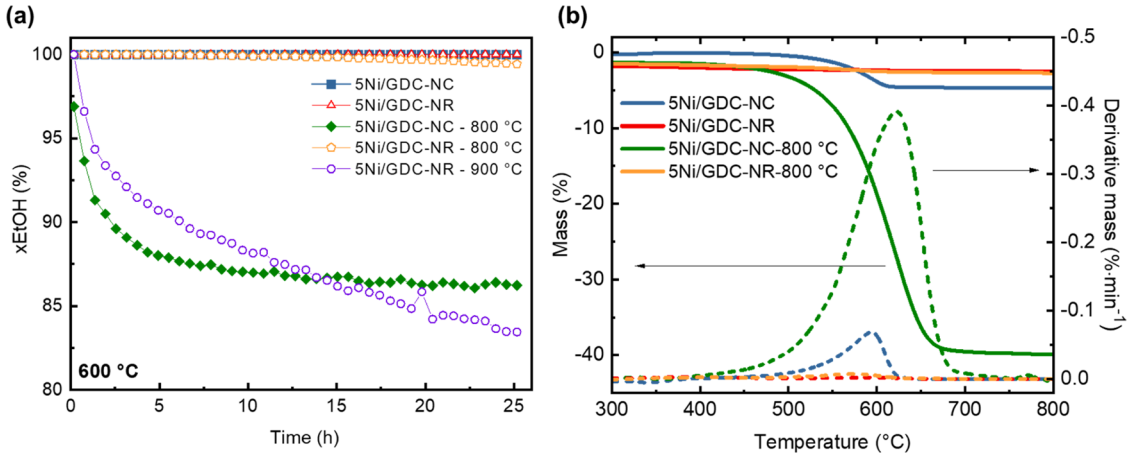

Figure 4. (a) Time on stream dependence of the ethanol conversion rate for the catalysts during ethanol steam reforming reactions at 600 °C. H_2O/ethanol molar ratio 3/1. (b) TGA mass loss of spent 5Ni/GDC-NC and 5Ni/GDC-NR catalysts after ESR at 600 °C.

3.2. ESR. The ethanol conversion as a function of time on stream (TOS) obtained for the ESR reactions at 600 °C is shown in Figure 4a. The reaction temperature of 600 °C was chosen as at this temperature coke deposition is favored,[48] and gas phase reactions are not active for ethanol dehydrogenation;[49] hence, it is preferred to evaluate catalytic activity. Moreover, to carefully evaluate the properties of the catalysts emulating the thermal history of an SOFC catalytic layer, the as-prepared catalysts were reduced at 450 °C, the temperature by which all Ni is reduced, as seen in Figure 1b, whereas the catalysts that were submitted to an additional heat treatment were reduced at 800 °C, which is a typical temperature for SOFC anode in situ reduction.

The as-prepared samples of NR and NC catalysts exhibit similar results because the impregnation method of Ni yields highly active small particles that inhibit coke formation during ESR. Both as-prepared catalysts (without heat treatment) showed 100% ethanol conversion during 25 h of reaction. However, the heat treatment at 800 °C resulted in striking differences in the catalytic properties of the samples. The nanorod supported catalyst (5Ni/GDC-NR) was practically unchanged after heating at 800 °C, sustaining 100% conversion of ethanol upon 15 h of TOS and a very small deactivation with increasing reaction time (~99% at 25 h). Additional ESR stability tests carried out at 700 °C showed excellent stable performance of 5Ni/GDC-NR treated at 800 °C (Figure S1). On the other hand, nanocubes exhibited a different behavior; heating the 5Ni/GDC-NC catalyst at 800 °C caused a fast deactivation, which decreased the ethanol conversion from 97% to 87% in the initial 5 h of reaction. Further increases in TOS had no effect on the 87% conversion, indicating that the catalyst preserved some activity. The 5Ni/GDC-NR catalyst heated at 900 °C showed 100% initial conversion of ethanol, but a fast deactivation in the initial five h of reaction, followed by a continuous loss of activity with increasing TOS, dropped the conversion rate to ~83% after 25 h.

The results shown in Figure 4a indicate that the 5Ni/GDC-NR remains active after heat treatment at 800 °C because of

https://doi.org/10.1021/acsaem.3c02757
ACS Appl. Energy Mater. 2024, 7, 1766−1776

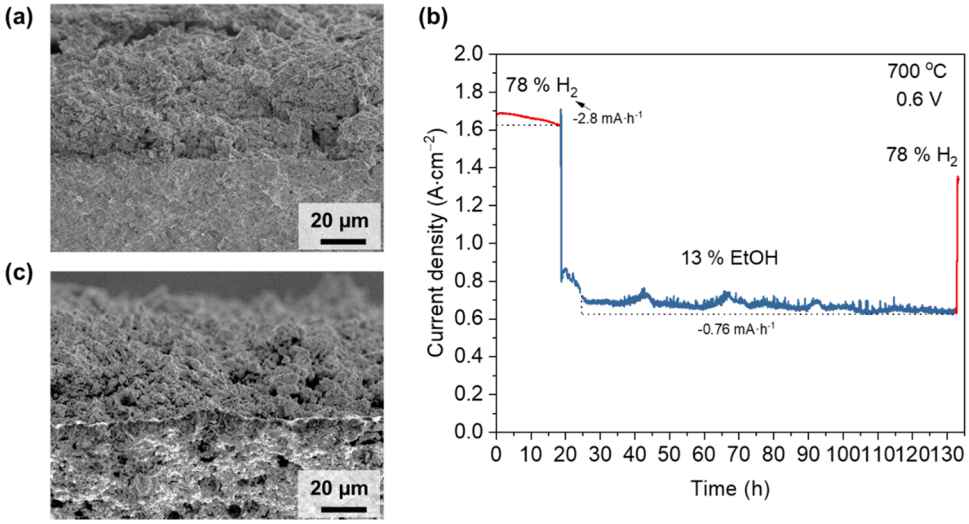

Figure 5. (a) Secondary electron SEM image of a fractured surface of the 5Ni/GDC-NR catalytic layer deposited on the anode and heated at 800 °C, (b) durability test under dry ethanol of the anode-supported single cell with the 5Ni/GDC-NR catalytic layer, 130 h at 700 °C, applied voltage of 0.6 V, and (c) SEM image of the fractured surface of the 5Ni/GDC-NR catalytic layer after the durability test.

the properties of the NR substrate, which allows a higher dispersion and stronger interaction with the impregnated Ni nanoparticles. Such features are possibly related to the higher initial surface area of the GDC-NR and the dispersion of Ni in the defective surface of the nanorods. At 800 °C, coarsening of the active sites is inhibited in the NR sample as the GDC nanorod support keeps a high surface area and a defective surface with pinning sites that anchor Ni nanoparticles, contributing to their high activity even if some coarsening of the NR support occurs. However, due to surface properties of the NRs, such nanoparticles were reported to exhibit a maximum sintering activity at T ∼ 800 °C.[33,50] Indeed, increasing the heat treatment temperature of the 5Ni/GDC-NR catalyst to 900 °C promotes a significant change from rods to fully crystallized rounded particles (Figure 2e). Such a change is associated with a loss in the capacity of anchoring the Ni nanoparticles and, therefore, diffusion of the metal occurs decreasing the dispersion of active sites and causing activity loss. It is interesting to note that the morphological changes of the 5Ni/GDC-NR after heating at 900 °C are different from that of the 5Ni/GDC-NC catalyst heated at 800 °C because the nanocubes are considerably less affected by the heat treatment than rods.[33] The GDC-NC support heated at 800 °C practically retains both the morphology and surface area of the as-prepared 5Ni/GDC-NC catalyst; thus, morphological changes in the metal nanoparticles are likely to dominate the loss of catalytic activity of the GDC-NC supported catalyst. The relatively low specific surface area and the morphology of the nanocubes inhibit a high dispersion of Ni nanoparticles (Figure 3a), favoring coarsening of the metallic particles in the edges of the nanocubes upon heating.

Interestingly, results in Figures 4a and S1 are considerably different from recently reported data of ESR because Ni/GDC catalysts sustained conversion rates well above the H2 thermodynamic equilibrium (∼40%), while no homogeneous reaction is expected at 600 °C.[48] As morphological changes of the Ni/GDC catalysts previously treated at higher temperatures are unlikely to take place at the reaction temperature (600 °C), the loss of activity in such conditions is possibly related to a solid carbon deposit that does not entirely cover the surface of the Ni active sites. Thus, some carbon accumulates at the surface of the catalysts treated at 800 and 900 °C without suppressing the catalytic activity possibly due to the oxygen transport and storage properties of GDC.

Figure 4b shows the thermogravimetric analysis (TGA) of spent catalysts carried out to investigate possible carbon formation in the catalysts' surface during ESR at 600 °C. The characteristics of the carbon deposit are reflected in the temperature range in which the corresponding mass loss is detected. Polymeric and filamentary carbon typically burn below 450 °C and above 550 °C, respectively, whereas more crystallized graphitic structures are observed to oxidized at temperatures above 700 °C.[36,51,52] The peaks in the derivative of mass loss develop between 620 and 590 °C indicating the oxidation of filamentous carbonaceous species.[36,51,53] The as-prepared 5Ni/GDC-NC catalyst presented a small mass loss of 5%, while the same catalyst after heat treatment at 800 °C showed the highest mass loss (40%). The as-prepared 5Ni/GDC-NR catalyst exhibited no mass loss indicating the absence of carbon deposits, while heating at 800 °C resulted in a small peak at 575 °C. These results are consistent with the ethanol conversion data (Figure 4a), in which the catalyst 5Ni/GDC-NC heat treated at 800 °C showed activity loss. The TGA data confirm that the deactivation of the catalyst was caused by carbon deposit formation, a feature more likely to occur in catalyst displaying low surface area and low metal dispersion.

Based on the experimental results of ESR, the 5Ni/GDC-NR catalyst was chosen for testing as a catalytic layer in a direct ethanol SOFC.

3.3. Direct Ethanol Fuel Cell Testing. Figure 5a shows the 5Ni/GDC-NR catalytic layer deposited and attached to the anode by heating to 800 °C. A total thickness of 50 μm was obtained for the catalytic layer by depositing 7 mg·cm^{-2} of the as-prepared 5Ni/GDC-NR catalyst ink. The SEM image shows that by heating at 800 °C the nanorod shape is lost in the sintered catalytic layer. This behavior is different from that observed after the heat treatment carried out on loose catalyst powder, in which coarser rods are still discerned as shown in Figure 2d and 3b. Such a feature is probably related to the packing of nanorods on the deposited layer that favors particle sintering and confirms the previously reported high sintering

https://doi.org/10.1021/acsaem.3c02757
ACS Appl. Energy Mater. 2024, 7, 1766−1776

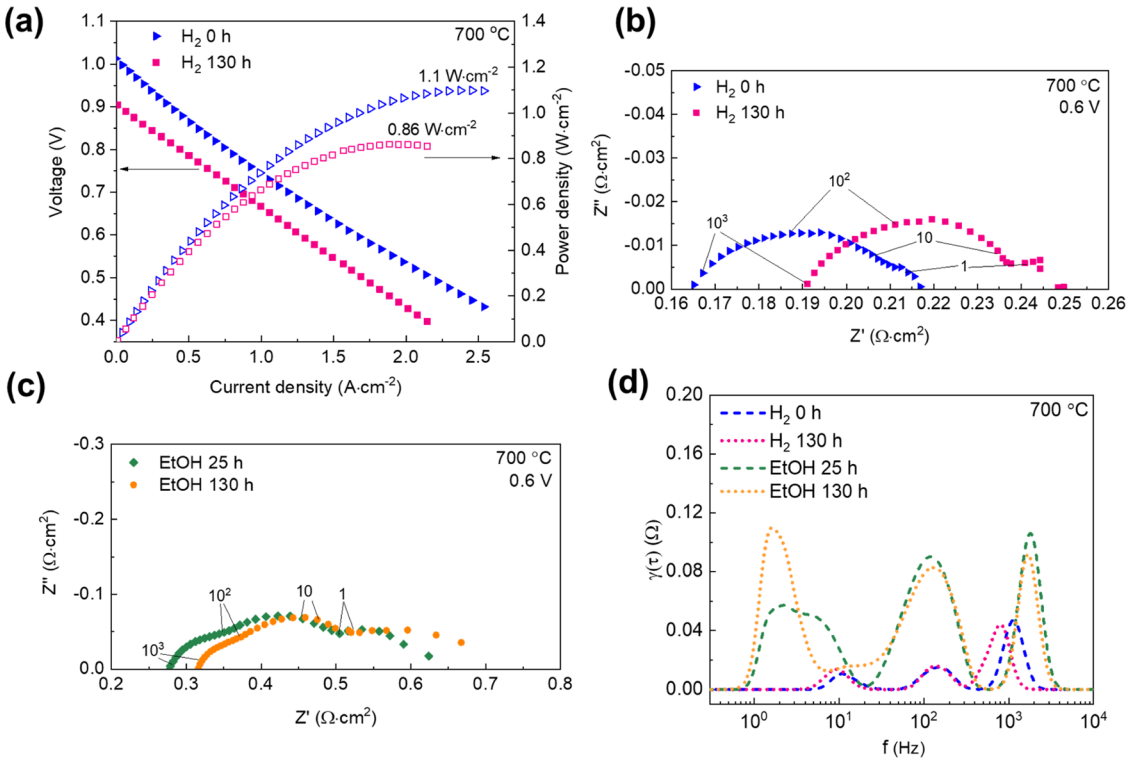

Figure 6. Electrochemical characterization of the fuel cell before and after the durability test of 130 h (20 h H_2 and 110 h EtOH) at 700 °C under 0.6 V polarization: (a) *I*–*V* curve under hydrogen and (b) impedance spectroscopy diagrams at 0.6 V under hydrogen, (c) impedance spectroscopy diagrams at 0.6 V under EtOH and (d) DRT analysis of the EIS spectra at 0.6 V under H_2 and EtOH.

activity of the nanorods.[32] Nevertheless, sintering at 800 °C resulted in a good adhesion of the catalytic layer to the anode support, and the sintering condition was used for the application of the catalytic layer to the commercial anode-supported fuel cell.

To investigate the effect of the catalytic layer on the electrochemical performance of fuel cells directly fed with anhydrous ethanol, a durability test was carried out at 700 °C and 0.6 V (Figure 5b). Initially, hydrogen was used as a fuel, and then it was changed to dry ethanol. No additional water was added to the fuel inlet aiming to study the stability of the catalyst for ethanol reforming using the water supplied by the H_2 electrochemical oxidation in the anode.[13,14]

After anode reduction and initial electrochemical measurements under hydrogen, the fuel cell was polarized at 0.6 V. Under hydrogen, the commercial fuel cell experienced a relatively fast degradation rate of −2.8 mA·h^{-1} at 0.6 V, and after ∼20 h, fuel was changed to dry ethanol. By changing the fuel to ethanol, the current output dropped from ∼1.6 A·cm^{-2} (H_2) to ∼0.8 A·cm^{-2}. Such a performance decrease can be related to the complex reactions taking place at both the anode and catalytic layer of the direct ethanol fuel cell. The Faradaic efficiency for ethanol conversion is lower than that of H_2 because the larger molecule size of ethanol imposes restrictions to mass transport in the porous layers. It is necessary to consider that the catalytic conversion of ethanol is limited to ∼70% of selectivity to hydrogen and other products are formed in the catalytic layer (see Figure S1). Nonetheless, simply assuming that the results of the packed bed catalytic reactor are directly related to the ones obtained in the fuel cell test rig oversimplifies important differences between these systems such as gas diffusion pathways and spatial velocity. Thus, the decreased current output in ethanol as compared to H_2 may be related to several parameters that require further experiments to be elucidated.

More importantly, the current output of the fuel cell under dry ethanol stabilizes at 0.65 A·cm^{-2} and remains practically stable during the test. After completing >110 h under ethanol, the fuel is changed back to hydrogen and the current increases to 1.4 A·cm^{-2}. It is interesting to note that a simple linear extrapolation of the initial degradation ratio under H_2 to 130 h of operation results in a final current close to 1.4 A·cm^{-2}, indicating that operation under ethanol promoted no additional degradation of the fuel cell. Moreover, it is important to consider that degradation due to carbon deposit is likely to occur within considerably shorter time interval than that of the stability test (<110 h).[10,48] Such an excellent result demonstrates that the active catalyst Ni-GDC-NR is capable of sustaining ethanol steam reforming at 700 °C using the water produced by the electrochemical oxidation of the H_2 generated by the ESR. Thus, both the catalytic and electrochemical reactions sustain each other without noticeable degradation due to coking. Furthermore, in the SEM image of the interface between anode and catalytic layer of fractured cell after the durability test (Figure 5c), there is no sign of delamination between the layers nor carbon deposits, filaments, or whiskers. It is interesting to note that carbon formation is expected at 700 °C for water/ethanol ratio (W/E) < 3, whereas the Ni/YSZ anode deactivates within minutes in ESR conditions with W/E = 3.[48] Therefore, it is possible to infer that the 5Ni/GDC-NR catalyst is highly active for ethanol conversion and that fuel utilization of the single cell provides enough water to sustain the ESR.

Polarization curves and EIS data were collected during the durability test and are shown in Figure 6. Additionally, the polarization curve under ethanol is shown in Figure S2. At the

https://doi.org/10.1021/acsaem.3c02757
ACS Appl. Energy Mater. 2024, 7, 1766−1776

beginning of the test, under H_2, the cell has an OCV = 1.04 V, with a rather linear $I-V$, indicating ohmic polarization as the main irreversibility, and a maximum power density of 1.10 W·cm^{-2} at 0.46 V, as shown in the $I-V$ curve in Figure 6a. The $I-V$ curve under H_2 measured after the ethanol durability test shows a decrease in the OCV (0.9 V), while preserving a rather linear behavior. The observed behavior is also reflected in the ethanol polarization curve (Figure S2). A partial oxidation of nickel during the ethanol test could reduce the OCV as the Ni-NiO equilibrium is ∼0.6 V. However, such a decrease in the OCV is possibly related to the presence of other ESR products, such as CH_4, CO, and CO_2 and, eventually, some carbon deposits that contribute to parallel reactions along with the H_2-H_2O equilibrium.

The EIS data can be used to further understand the electrochemical behavior of the fuel cell by separating the series (R_s) and polarization resistances (R_p). The EIS diagrams under 0.6 V polarization taken during the stability test are shown in Figure 6b,c under H_2 and ethanol, respectively, and the corresponding DRT analyses are shown in Figure 6d. Under H_2, the R_s attributed to the ohmic resistance is the main component (∼70%) of the total resistance of the fuel cell. The DRT analysis of the R_p components provides a deeper understanding of electrode reactions. Three relaxations can be separated at ∼10^3, 10^2, and 10 Hz, in agreement with typical results for anode-supported cells.[54,55] The largest contribution is at 10^3 Hz, usually attributed to charge transfer phenomena and ionic transport.[55] The relaxations at 10^2 and 10 Hz are related to electrode processes, usually, cathodic adsorption/desorption and transport of ionic species, and anodic mass diffusion occurring at the low frequency end of the diagrams, respectively.[54−56] After the durability test (130 h), the DRT under H_2 exhibited no significant changes. Peaks at 10^3 and 10 Hz are slightly shifted to lower frequencies, indicating that the charge transfer process and low frequency mass diffusion process are slightly retarded after the durability test. Such features can be related to both electrochemical degradation of the fuel cell, in the high frequency activation polarization, and to a microstructural degradation of the anode. Such anodic degradation is reflected in the low frequency range relaxation and can be related to either coarsening of the YSZ/NiO anode and eventual blocking of diffusion paths due to accumulation of ESR products and possible small carbon deposits. Nevertheless, the EIS data suggest that the electrodes had little degradation after 110 h operating under ethanol. It is interesting to note that the observed increase of the total resistance after the durability test is mostly due to an increase in the R_s value, while R_p was considerably less affected.

The EIS diagrams collected under ethanol are markedly different from those in H_2 (Figure 6c). By comparison of the EIS data in Figure 6b,c, the resistances extracted from impedance diagrams measured at the beginning of the test for both H_2 (t = 0 h) and ethanol (t = 25 h) show important features. A pronounced increase of the R_s value from 0.15 to 0.27 Ω·cm^2 is observed when fuel is changed from H_2 to ethanol, in agreement with the decreased current output under ethanol. Such R_s and R_p increase in ethanol can be related to a local decrease of the fuel cell temperature due to the endothermic nature of the ESR reaction.[57] There is a considerable increase of R_p when comparing the R_p = 0.06 Ω·cm^2 under H_2 (t = 0 h) and 0.27 Ω·cm^2 under ethanol (t = 25 h). The DRT analysis under ethanol (Figure 6d) reveals basically the same three polarization components shifted in frequency and, more notably, with a higher magnitude than in H_2. The largest R_p increase is observed for the components at intermediary (∼10^2 Hz), which is reported to be temperature dependent, and low (∼1 to 10 Hz) frequencies. The low frequency contributions are usually temperature independent and associated with gas diffusion in the anode substrate, and it is noticeable that by changing the fuel from H_2 to ethanol, there is a significant shift in the anode gas diffusion contribution to lower frequencies, which is likely associated with the diffusion of the large unreformed ethanol molecules and fuel dilution by other products of the ESR reaction.[55,56,58] It is interesting to note that the EIS data in ethanol revealed no significant electrode degradation after the durability test. The relatively small increase in both R_s and R_p agrees with the rather stable performance of the fuel cell on dry ethanol. Indeed, by comparing DRT analysis for EIS data under ethanol at t = 25 h and t = 130 h, there is an increase in the lowest frequency peak, whereas the other peaks remain unchanged. The mass diffusion component becomes the largest contribution to the polarization resistance of the fuel cell operating under ethanol. The increase in this contribution can be associated with both the complex reactions taking place in the anode and a partial deactivation of the catalytic layer. It is important to consider that the fuel cell was tested in harsh conditions relaying on the catalytic properties of the Ni/GDC-NR to convert ethanol using the water generated in the anode by the hydrogen electrochemical oxidation, and carbon formation can occur in the YSZ/Ni anode in ethanol steam reforming at 700 °C at reduced W/E <3 ratio.[48] The measured performance decay during operation under hydrogen reduces the fuel utilization factor, which decreases the water generated and may result in a deficient W/E ratio for stable ESR at 700 °C. Nonetheless, the deactivation of the catalytic layer did not appear to have a significant effect on the anode, as shown in Figure 6b,c, where the main contribution to the degradation of the cell is due to the increase in the ohmic resistance R_s. Nevertheless, the experimental result indicated that a rather stable operation in ethanol was achieved, wherein some carbon is partially formed on the support surface without a significant accumulation that suppresses the activity.

4. CONCLUSIONS

Catalysts comprising controlled shaped, nanocubes and nanorods and GDC supports with impregnated Ni (Ni/GDC) were found to be highly active for ethanol steam reforming reaction at intermediate temperature (600−700 °C). The morphology of the support had a striking effect on the catalytic properties of the Ni/GDC upon heat treatments at the typical processing and operating temperatures of a solid oxide fuel cell. The GDC nanocubes have comparatively lower surface area than the nanorods, and cubic faces were observed to poorly support impregnated metallic nanoparticles, which tend to cluster at the edges of the cubes. Thus, upon heat treatment at 800 °C nanocubes retain their shape and surface area, while a fast degradation of the catalytic properties due to coarsening of the active Ni sites occurs. Differently, the high surface area of the GDC nanorods, with highly defective surface, is known to promote mass diffusion processes at relatively low temperature but also to provide high dispersion and anchoring of the Ni active particles. Therefore, the catalytic properties are less sensitive to the heating of the nanorod catalyst up to 800 °C. Nonetheless, upon heating at 900 °C, nanorods show a pronounced sintering, changing the

https://doi.org/10.1021/acsaem.3c02757
ACS Appl. Energy Mater. 2024, 7, 1766−1776

shape of the support and favoring the Ni agglomeration and deactivation. The fuel cell using the Ni/GDC-nanorod catalytic layer sintered at 800 °C showed a stable performance for more than 100 h of continuous operation under dry ethanol at 700 °C. Both the electrochemical characterization and post-test analysis indicate no significant degradation due to coking, confirming that the highly active Ni/GDC catalyst is a promising catalytic layer for intermediate temperature direct ethanol solid oxide fuel cell.

■ ASSOCIATED CONTENT

Supporting Information

The Supporting Information is available free of charge at https://pubs.acs.org/doi/10.1021/acsaem.3c02757.

Time dependence of the product distribution of ethanol steam reforming and ethanol fuel cell power density curves (PDF)

■ AUTHOR INFORMATION

Corresponding Author

Fabio C. Fonseca − *Nuclear and Energy Research Institute (IPEN-CNEN), 05508-000 São Paulo, SP, Brazil;* orcid.org/0000-0003-0708-2021; Email: fabiocf@usp.br

Authors

Marina Machado − *Nuclear and Energy Research Institute (IPEN-CNEN), 05508-000 São Paulo, SP, Brazil; Centre for Engineering, Modelling and Applied Social Sciences, Federal University of ABC (UFABC), 09210-580 Santo André, SP, Brazil*

Lays N. Rodrigues − *Nuclear and Energy Research Institute (IPEN-CNEN), 05508-000 São Paulo, SP, Brazil*

Vanessa B. Vilela − *Nuclear and Energy Research Institute (IPEN-CNEN), 05508-000 São Paulo, SP, Brazil;* orcid.org/0000-0001-9281-3233

Tamara S. Moraes − *Nuclear and Energy Research Institute (IPEN-CNEN), 05508-000 São Paulo, SP, Brazil*

Andre S. Ferlauto − *Centre for Engineering, Modelling and Applied Social Sciences, Federal University of ABC (UFABC), 09210-580 Santo André, SP, Brazil;* orcid.org/0000-0003-3056-7289

Complete contact information is available at: https://pubs.acs.org/10.1021/acsaem.3c02757

Notes

The authors declare no competing financial interest.

■ ACKNOWLEDGMENTS

The authors would like to acknowledge the support of the Comissão Nacional de Energia Nuclear (IPEN-CNEN) and the Brazilian agencies FAPESP grant nos 2017/11937-4, 2019/04499-6, 2019/15110-2, 2022/06295-1, and CNPq Sis-H2 407967/2022-2. F.C.F. and A.S.F. are CNPq fellows. The LNNano (20230736) is acknowledged.

■ REFERENCES

(1) Park, S.; Vohs, J. M.; Gorte, R. J. Direct Oxidation of Hydrocarbons in a Solid-Oxide Fuel Cell. *Nature* **2000**, *404* (6775), 265−267.

(2) Laosiripojana, N.; Assabumrungrat, S. Catalytic Steam Reforming of Methane, Methanol, and Ethanol over Ni/YSZ: The Possible Use of These Fuels in Internal Reforming SOFC. *J. Power Sources* **2007**, *163* (2), 943−951.

(3) Hotza, D.; Diniz da Costa, J. C. Fuel Cells Development and Hydrogen Production from Renewable Resources in Brazil. *Int. J. Hydrogen Energy* **2008**, *33* (19), 4915−4935.

(4) Farrell, B.; Linic, S. Direct Electrochemical Oxidation of Ethanol on SOFCs: Improved Carbon Tolerance of Ni Anode by Alloying. *Appl. Catal., B* **2016**, *183*, 386−393.

(5) de Lima, S. M.; da Silva, A. M.; da Costa, L. O. O.; Graham, U. M.; Jacobs, G.; Davis, B. H.; Mattos, L. V.; Noronha, F. B. Study of Catalyst Deactivation and Reaction Mechanism of Steam Reforming, Partial Oxidation, and Oxidative Steam Reforming of Ethanol over Co/CeO2 Catalyst. *J. Catal.* **2009**, *268* (2), 268−281.

(6) Vargas, J. C.; Libs, S.; Roger, A.-C.; Kiennemann, A. Study of Ce-Zr-Co Fluorite-Type Oxide as Catalysts for Hydrogen Production by Steam Reforming of Bioethanol. *Catal. Today* **2005**, *107*−*108*, 417−425.

(7) Compagnoni, M.; Tripodi, A.; Di Michele, A.; Sassi, P.; Signoretto, M.; Rossetti, I. Low Temperature Ethanol Steam Reforming for Process Intensification: New Ni/MxO−ZrO_2 Active and Stable Catalysts Prepared by Flame Spray Pyrolysis. *Int. J. Hydrogen Energy* **2017**, *42* (47), 28193−28213.

(8) da Silva, A. A. A.; Bion, N.; Epron, F.; Baraka, S.; Fonseca, F. C.; Rabelo-Neto, R. C.; Mattos, L. V.; Noronha, F. B. Effect of the Type of Ceria Dopant on the Performance of Ni/CeO2 SOFC Anode for Ethanol Internal Reforming. *Appl. Catal., B* **2017**, *206*, 626−641.

(9) Muccillo, R.; Muccillo, E. N. S.; Fonseca, F. C.; Florio, D. Z. de. Characteristics and Performance of Electrolyte-Supported Solid Oxide Fuel Cells under Ethanol and Hydrogen. *J. Electrochem. Soc.* **2008**, *155* (3), B232.

(10) Chang, H.; Chen, H.; Yang, G.; Zhou, W.; Bai, J.; Li, S.; Shao, Z. Enhanced Coking Resistance of a Ni Cermet Anode by a Chromates Protective Layer. *J. Energy Chem.* **2019**, *37*, 117−125.

(11) Livinalli, M. M. Development of Functional Layers for Direct Ethanol Solid Oxide Fuel Cells. PhD Thesis. Universidade de São Paulo: São Paulo, 2022.

(12) Monteiro, N. K.; Noronha, F. B.; da Costa, L. O. O.; Linardi, M.; Fonseca, F. C. A Direct Ethanol Anode for Solid Oxide Fuel Cell Based on a Chromite-Manganite with Catalytic Ruthenium Nanoparticles. *Int. J. Hydrogen Energy* **2012**, *37* (12), 9816−9829.

(13) Steil, M. C.; Nobrega, S. D.; Georges, S.; Gelin, P.; Uhlenbruck, S.; Fonseca, F. C. Durable Direct Ethanol Anode-Supported Solid Oxide Fuel Cell. *Appl. Energy* **2017**, *199*, 180−186.

(14) Nobrega, S. D.; Galesco, M. V.; Girona, K.; de Florio, D. Z.; Steil, M. C.; Georges, S.; Fonseca, F. C. Direct Ethanol Solid Oxide Fuel Cell Operating in Gradual Internal Reforming. *J. Power Sources* **2012**, *213*, 156−159.

(15) Zhang, P.; Yang, Z.; Jin, Y.; Liu, C.; Lei, Z.; Chen, F.; Peng, S. Progress Report on the Catalyst Layers for Hydrocarbon-Fueled SOFCs. *Int. J. Hydrogen Energy* **2021**, *46* (79), 39369−39386.

(16) Zhang, P.; Hu, L.; Zhao, B.; Lei, Z.; Ge, B.; Yang, Z.; Jin, X.; Peng, S. Direct Power Generation from Ethanol by Solid Oxide Fuel Cells with an Integrated Catalyst Layer. *Fuel* **2023**, *333*, No. 126340.

(17) Zhurka, M. D.; Lemonidou, A. A.; Kechagiopoulos, P. N. Elucidation of Metal and Support Effects during Ethanol Steam Reforming over Ni and Rh Based Catalysts Supported on (CeO_2)-ZrO_2-La_2O_3. *Catal. Today* **2021**, *368*, 161−172.

(18) Hou, T.; Yu, B.; Zhang, S.; Xu, T.; Wang, D.; Cai, W. Hydrogen Production from Ethanol Steam Reforming over Rh/CeO_2 Catalyst. *Catal. Commun.* **2015**, *58*, 137−140.

(19) Zhang, B.; Tang, X.; Li, Y.; Cai, W.; Xu, Y.; Shen, W. Steam Reforming of Bio-Ethanol for the Production of Hydrogen over Ceria-Supported Co, Ir and Ni Catalysts. *Catal. Commun.* **2006**, *7* (6), 367−372.

(20) Sharma, Y. C.; Kumar, A.; Prasad, R.; Upadhyay, S. N. Ethanol Steam Reforming for Hydrogen Production: Latest and Effective Catalyst Modification Strategies to Minimize Carbonaceous Deactivation. *Renewable Sustainable Energy Rev.* **2017**, *74*, 89−103.

(21) Ogo, S.; Sekine, Y. Recent Progress in Ethanol Steam Reforming Using Non-Noble Transition Metal Catalysts: A Review. *Fuel Process. Technol.* **2020**, *199*, No. 106238.

(22) Greluk, M.; Gac, W.; Rotko, M.; Słowik, G.; Turczyniak-Surdacka, S. Co/CeO_2 and Ni/CeO_2 Catalysts for Ethanol Steam Reforming: Effect of the Cobalt/Nickel Dispersion on Catalysts Properties. *J. Catal.* **2021**, *393*, 159−178.
(23) Vicente, J.; Ereña, J.; Olazar, M.; Benito, P. L.; Bilbao, J.; Gayubo, A. G. Kinetic Behaviour of Commercial Catalysts for Methane Reforming in Ethanol Steam Reforming Process. *J. Energy Chem.* **2014**, *23* (5), 639−644.
(24) Inaba, H. Ceria-Based Solid Electrolytes. *Solid State Ionics* **1996**, *83* (1−2), 1−16.
(25) Steele, B. Appraisal of $Ce_{1-y}Gd_yO_{2-y/2}$ Electrolytes for IT-SOFC Operation at 500°C. *Solid State Ionics* **2000**, *129* (1−4), 95−110.
(26) Ferreira, G. R.; Nogueira, F. G. E.; Lucrédio, A. F.; Assaf, E. M. Ethanol Steam Reforming by Ni Catalysts for H_2 Production: Evaluation of Gd Effect in CeO_2 Support. *Catal. Lett.* **2022**, *152*, 3125−3145, DOI: 10.1007/s10562-021-03875-3.
(27) Yang, S.; Zhou, F.; Liu, Y.; Zhang, L.; Chen, Y.; Wang, H.; Tian, Y.; Zhang, C.; Liu, D. Morphology Effect of Ceria on the Performance of CuO/CeO_2 Catalysts for Hydrogen Production by Methanol Steam Reforming. *Int. J. Hydrogen Energy* **2019**, *44* (14), 7252−7261.
(28) Araiza, D. G.; Gómez-Cortés, A.; Díaz, G. Effect of Ceria Morphology on the Carbon Deposition during Steam Reforming of Ethanol over Ni/CeO_2 Catalysts. *Catal. Today* **2020**, *349*, 235−243.
(29) Du, X.; Zhang, D.; Shi, L.; Gao, R.; Zhang, J. Morphology Dependence of Catalytic Properties of Ni/CeO_2 Nanostructures for Carbon Dioxide Reforming of Methane. *J. Phys. Chem. C* **2012**, *116* (18), 10009−10016.
(30) Soykal, I. I.; Bayram, B.; Sohn, H.; Gawade, P.; Miller, J. T.; Ozkan, U. S. Ethanol Steam Reforming over Co/CeO_2 Catalysts: Investigation of the Effect of Ceria Morphology. *Appl. Catal., A* **2012**, *449*, 47−58.
(31) Rodrigues, T. S.; de Moura, A. B. L.; e Silva, F. A.; Candido, E. G.; da Silva, A. G. M.; de Oliveira, D. C.; Quiroz, J.; Camargo, P. H. C.; Bergamaschi, V. S.; Ferreira, J. C.; Linardi, M.; Fonseca, F. C. Ni Supported $Ce_{0.9}Sm_{0.1}O_{2-\delta}$ Nanowires: An Efficient Catalyst for Ethanol Steam Reforming for Hydrogen Production. *Fuel* **2019**, *237*, 1244−1253.
(32) Moraes, T. S.; Neto, R. C. R.; Ribeiro, M. C.; Mattos, L. V.; Kourtelesis, M.; Verykios, X.; Noronha, F. B. Effects of Ceria Morphology on Catalytic Performance of Ni/CeO_2 Catalysts for Low Temperature Steam Reforming of Ethanol. *Top. Catal.* **2015**, *58* (4), 281−294.
(33) Esposito, V.; Kabir, A.; Rosa, M.; Nong, N. V.; Rodrigues, T. S.; Rodrigues, L. N.; Machado, M. F. S.; Moraes, L. P. R.; Marani, D.; Fonseca, F. C. Tuning Diffusion Paths in Shaped Ceria Nanocrystals. *CrystEngComm* **2019**, *21* (27), 4025−4029.
(34) Nobrega, S. D.; Gelin, P.; Georges, S.; Steil, M. C.; Augusto, B. L.; Noronha, F. B.; Fonseca, F. C. A Fuel-Flexible Solid Oxide Fuel Cell Operating in Gradual Internal Reforming. *J. Electrochem. Soc.* **2014**, *161* (3), F354.
(35) Liao, M.; Wang, W.; Ran, R.; Shao, Z. Development of a Ni−$Ce_{0.8}Zr_{0.2}O_2$ Catalyst for Solid Oxide Fuel Cells Operating on Ethanol through Internal Reforming. *J. Power Sources* **2011**, *196* (15), 6177−6185.
(36) da Silva, A. A. A.; Steil, M. C.; Tabuti, F. N.; Rabelo-Neto, R. C.; Noronha, F. B.; Mattos, L. V.; Fonseca, F. C. The Role of the Ceria Dopant on Ni/Doped-Ceria Anodic Layer Cermets for Direct Ethanol Solid Oxide Fuel Cell. *Int. J. Hydrogen Energy* **2021**, *46* (5), 4309−4328.
(37) Anelli, S.; Baiutti, F.; Hornés, A.; Bernadet, L.; Torrell, M.; Tarancón, A. Improved Mesostructured Oxygen Electrodes for Highly Performing Solid Oxide Cells for Co-Electrolysis of Steam and Carbon Dioxide. *J. Mater. Chem. A* **2019**, *7* (48), 27458−27468.
(38) Mai, H.-X.; Sun, L.-D.; Zhang, Y.-W.; Si, R.; Feng, W.; Zhang, H.-P.; Liu, H.-C.; Yan, C.-H. Shape-Selective Synthesis and Oxygen Storage Behavior of Ceria Nanopolyhedra, Nanorods, and Nanocubes. *J. Phys. Chem. B* **2005**, *109* (51), 24380−24385.
(39) Shi, W.; Song, S.; Zhang, H. Hydrothermal Synthetic Strategies of Inorganic Semiconducting Nanostructures. *Chem. Soc. Rev.* **2013**, *42* (13), 5714.
(40) Machado, M.; Rodrigues, L. N.; Vilela, V. B.; Ferlauto, A. S.; Moraes, T.; Fonseca, F. C. Shape-Controlled Ni Supported GDC Catalyst and Its Application in Direct Ethanol Solid Oxide Fuel Cells. *ECS Trans.* **2023**, *111* (6), 1463−1472.
(41) Wan, T. H.; Saccoccio, M.; Chen, C.; Ciucci, F. Influence of the Discretization Methods on the Distribution of Relaxation Times Deconvolution: Implementing Radial Basis Functions with DRTtools. *Electrochim. Acta* **2015**, *184*, 483−499.
(42) Roh, H. S.; Jun, K. W.; Dong, W. S.; Chang, J. S.; Park, S. E.; Joe, Y. I. Highly Active and Stable Ni/Ce-ZrO_2 Catalyst for H_2 Production from Methane. *J. Mol. Catal. A: Chem.* **2002**, *181* (1−2), 137−142.
(43) Gurav, H. R.; Dama, S.; Samuel, V.; Chilukuri, S. Influence of Preparation Method on Activity and Stability of Ni Catalysts Supported on Gd Doped Ceria in Dry Reforming of Methane. *J. CO_2 Util.* **2017**, *20*, 357−367.
(44) Yao, H. C.; Yao, Y. F. Y. Ceria in Automotive Exhaust Catalysts: I. Oxygen Storage. *J. Catal.* **1984**, *86* (2), 254−265.
(45) Silva, A. G. M.; Rodrigues, T. S.; Dias, A.; Fajardo, H. V.; Gonçalves, R. F.; Godinho, M.; Robles-Dutenhefner, P. A. $Ce_{1-x}Sm_xO_{1.9-\delta}$ Nanoparticles Obtained by Microwave-Assisted Hydrothermal Processing: An Efficient Application for Catalytic Oxidation of α-Bisabolol. *Catal. Sci. Technol.* **2014**, *4* (3), 814.
(46) Soykal, I. I.; Sohn, H.; Ozkan, U. S. Effect of Support Particle Size in Steam Reforming of Ethanol over Co/CeO_2 Catalysts. *ACS Catal.* **2012**, *2* (11), 2335−2348.
(47) Shi, G.; Chen, Q.; Zhang, Q.; Cai, W.; Li, Z.; Zhai, S.; Yu, H.; Tan, F.; Wang, Y. Morphology Effect of ZnO Support on the Performance of Cu toward Methanol Production from CO_2 Hydrogenation. *J. Saudi Chem. Soc.* **2020**, *24* (1), 42−51.
(48) Vicente, J.; Ereña, J.; Montero, C.; Azkoiti, M. J.; Bilbao, J.; Gayubo, A. G. Reaction Pathway for Ethanol Steam Reforming on a Ni/SiO_2 Catalyst Including Coke Formation. *Int. J. Hydrogen Energy* **2014**, *39* (33), 18820−18834.
(49) Donazzi, A.; Schmauss, T. A.; Barnett, S. A. Catalytic and Electrocatalytic Performance of $Sr(Ti_{0.3}Fe_{0.7}Ru_{0.07})O_{3-\delta}$ for Applications in Solid Oxide Fuel Cells Supplied with Ethanol Steam Reforming Mixtures. *J. Power Sources* **2022**, *551*, No. 232215.
(50) De Florio, D. Z.; Esposito, V.; Traversa, E.; Muccillo, R.; Fonseca, F. C. Master Sintering Curve for Gd-Doped CeO_2 Solid Electrolytes. *J. Therm. Anal. Calorim.* **2009**, *97* (1), 143−147.
(51) Ferlauto, A. S.; de Florio, D. Z.; Fonseca, F. C.; Esposito, V.; Muccillo, R.; Traversa, E.; Ladeira, L. O. Chemical Vapor Deposition of Multi-Walled Carbon Nanotubes from Nickel/Yttria-Stabilized Zirconia Catalysts. *Appl. Phys. A: Mater. Sci. Process.* **2006**, *84* (3), 271−276.
(52) Trigueiro, J. P. C.; Silva, G. G.; Lavall, R. L.; Furtado, C. A.; Oliveira, S.; Ferlauto, A. S.; Lacerda, R. G.; Ladeira, L. O.; Liu, J.-W.; Frost, R. L.; George, G. A. Purity Evaluation of Carbon Nanotube Materials by Thermogravimetric, TEM, and SEM Methods. *J. Nanosci. Nanotechnol.* **2007**, *7* (10), 3477−3486.
(53) Alberton, A. L.; Souza, M. M. V. M.; Schmal, M. Carbon Formation and Its Influence on Ethanol Steam Reforming over Ni/Al_2O_3 Catalysts. *Catal. Today* **2007**, *123* (1), 257−264.
(54) Osinkin, D. A. An Approach to the Analysis of the Impedance Spectra of Solid Oxide Fuel Cell Using the DRT Technique. *Electrochim. Acta* **2021**, *372*, No. 137858.
(55) Escudero, M. J.; Valero, C.; Cauqui, M. Á.; Goma, D.; Yeste, M. P. Ni-Ce-ZrO2 System as Anode Material for Direct Internal Reforming Biogas Solid Oxide Fuel Cells. *Fuel* **2022**, *322*, No. 124247.
(56) Dierickx, S.; Weber, A.; Ivers-Tiffée, E. How the Distribution of Relaxation Times Enhances Complex Equivalent Circuit Models for Fuel Cells. *Electrochim. Acta* **2020**, *355*, No. 136764.
(57) Dogdibegovic, E.; Fukuyama, Y.; Tucker, M. C. Ethanol Internal Reforming in Solid Oxide Fuel Cells: A Path toward High

Performance Metal-Supported Cells for Vehicular Applications. *J. Power Sources* **2020**, *449*, No. 227598.
(58) Kromp, A.; Dierickx, S.; Leonide, A.; Weber, A.; Ivers-Tiffée, E. Electrochemical Analysis of Sulfur-Poisoning in Anode Supported SOFCs Fuelled with a Model Reformate. *J. Electrochem. Soc.* **2012**, *159* (5), B597−B601.

https://doi.org/10.1021/acsaem.3c02757
ACS Appl. Energy Mater. 2024, 7, 1766−1776